INTERNATIONAL JOURNAL FOR NUMERICAL METHODS IN FLUIDS, VOL. 24, 1159–1183 (1997)

NUMERICAL SIMULATIONS OF LAMINAR FLOW OVER A 3D BACKWARD-FACING STEP

P. T. WILLIAMS[1]* AND A. J. BAKER[2]

[1] *Computational Physics and Engineering Division, Oak Ridge National Laboratory, Oak Ridge, TN 37831, U.S.A.*
[2] *Department of Engineering Science and Mechanics, University of Tennessee, Knoxville, TN 37996, U.S.A.*

SUMMARY

A numerical investigation of laminar flow over a three-dimensional backward-facing step is presented with comparisons with detailed experimental data, available in the literature, serving to validate the numerical results. The continuity constraint method, implemented via a finite element weak statement, was employed to solve the unsteady three-dimensional Navier–Stokes equations for incompressible laminar isothermal flow. Two-dimensional numerical simulations of this step geometry underestimate the experimentally determined extent of the primary separation region for Reynolds numbers *Re* greater than 400. It has been postulated that this disagreement between physical and computational experiments is due to the onset of three-dimensional flow near $Re \approx 400$. This paper presents a full three-dimensional simulation of the step geometry for $100 \leqslant Re \leqslant 800$ and correctly predicts the primary reattachment lengths, thus confirming the influence of three-dimensionality. Previous numerical studies have discussed possible instability modes which could induce a sudden onset of three-dimensional flow at certain critical Reynolds numbers. The current study explores the influence of the sidewall on the development of three-dimensional flow for $Re > 400$. Of particular interest is the characterization of three-dimensional vortices in the primary separation region immediately downstream of the step. The complex interaction of a wall jet, located at the step plane near the sidewall, with the mainstream flow reveals a mechanism for the increasing penetration (with increasing Reynolds number) of three-dimensional flow structures into a region of essentially two-dimensional flow near the midplane of the channel. The character and extent of the sidewall-induced flow are investigated for $100 \leqslant Re \leqslant 800$. © 1997 by John Wiley & Sons, Ltd.

Int. J. Numer. Meth. Fluids, **24**: 1159–1183, 1997.

No. of Figs: 20 No. of Tables: 1 No. of Refs: 42.

KEY WORDS: backward-facing step; laminar flow; Navier–Stokes; finite elements; 3D

1. INTRODUCTION

As a subject of fundamental importance in fluid mechanics, flow separation has been the focus of intensive study for many years. To aid in experimental and computational investigations of this phenomenon, a set of simple geometric configurations has been developed as representative test beds, including (a) flow in a pipe with a sudden expansion, (b) flow in a pipe with an obstruction such as an orifice, (c) flow over an obstruction (either a step or a thin fence) in a channel and (d) flow in channel with a sudden expansion (backward-facing step). Within each base configuration, variations in boundary conditions and the addition of heat and/or mass transfer serve to further broaden the

* Correspondence to: P. T. Williams.

CCC 0271–2091/97/111159–25 $17.50

Received 26 September 1994
Revised 7 December 1995

problem class. Among these four basic configurations the backward-facing step has become a very popular benchmarking and validation test problem for computational fluid dynamics (CFD) simulations owing to its simple geometry and the availability of quality experimental data. It is the objective of the current study to investigate laminar flow over a three-dimensional backward-facing step. Using the step geometry and flow conditions reported by Armaly *et al.*,[1] direct comparisons with the physical experiments are made as a validation of the numerical results.

Flow separation can be defined as a region of recirculating flow adjacent to a solid boundary. The positions for detachment and reattachment of the 'separation bubble' are delimited by contours of zero vorticity near the boundary. Within the separation bubble the flow is characterized by recirculating vortices and flow reversals. A necessary but not sufficient condition for the onset of flow separation in both boundary layer and fully viscous flows is the presence of an adverse pressure gradient in the flow field near the outer boundary of the separation bubble, where 'adverse' refers to an increasing pressure in the direction of the main flow stream.[2]

Axisymmetric flow with a sudden enlargement has been the subject of computational studies by Baker,[3] Donea *et al.*,[4] Zienkiewicz *et al.*,[5] and Fang and Paraschivoiu.[6] Laminar experimental data for this configuration were obtained by Leone and Gresho[7] and Carvalho *et al.*[8] Turbulent and laminar stratified channel flow with a backward-facing step has been studied computationally by Oliver,[9] Leone,[10] Gartling[11] and Papanastasiou *et al.*[12] Kaiktsis *et al.*[13] investigated the onset of three-dimensionality and transition to turbulence for flow over a backward-facing step using a high-order-accurate mixed spectral/spectral element method. For most of their cases, periodic boundary conditions were applied to the sidewalls of the models, thus simulating a channel geometry infinite in extent in the cross-stream direction. In the absence of sidewall effects, Kaiktsis *et al.*[13] found that the 'onset of three-dimensionality occurs at the boundaries between the primary and secondary recirculating zones with the main channel flow, . . .'. Strong secondary instabilities were observed in the shear layers, mainly due to an instability emanating from the step corner.

The present study has concentrated on isothermal three-dimensional internal laminar flows over a backward-facing step. Two experimental investigations have been used extensively in validation efforts quoted in the literature, specifically the laminar data of Denham and Patrick[14] and the laminar and turbulent data of Armaly *et al.*[1]

Computational simulations of the step geometry used by Denham and Patrick[14] have consistently predicted longer reattachment lengths for the primary separation bubble than those obtained experimentally.[15,16] This discrepancy has been attributed to the construction of the test section, which included an asymmetric flared device along the lower wall of the channel upstream of the step. Ghia *et al.*[16] observe that, since the resulting inlet section was relatively short, the velocity profiles obtained by Denham and Patrick[14] just before the step indicate an asymmetric distortion from the parabolic profiles typically assumed in computational studies. The severity of this distortion increases with increasing Reynolds number.

An open-loop air-driven flow channel was used by Armaly *et al.*[1] to measure velocity distributions and reattachment lengths downstream of a backward-facing step (see Figure 1). Results are presented for laminar, transitional and turbulent flow of air with a Reynolds number range of $70 < Re < 8000$. The channel height upstream of the step, h, was 5·2 mm and the downstream channel height H was 10·1 mm, giving an expansion ratio $H/h = 1{\cdot}9423$ and a step height S of 4·9 mm. The channel width W was 180 mm and $W/S = 36{\cdot}735$. The test section provided a 200 mm straight channel approach to the backward-facing step and a 500 mm long channel downstream of the step. Operating in a forward-scattering mode, the laser Doppler anemometer was set up to measure only the streamwise velocity component.

The reattachment lengths of the separation regions were measured by scanning the lower and upper walls in the streamwise direction at constant and known elevations. To determine the reattachment

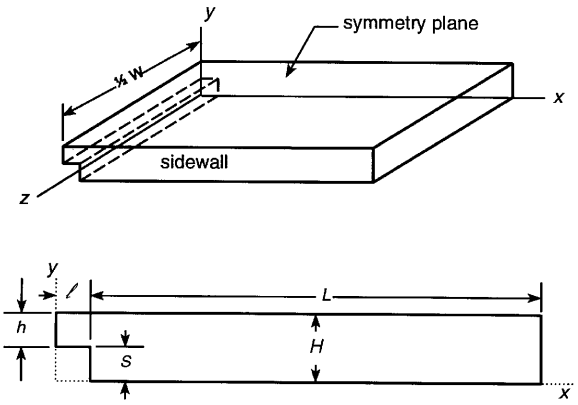

Figure 1. Backward-facing step geometry

length, the position of the zero-mean-velocity line was measured. The points of detachment and reattachment were taken as the extrapolated zero-velocity line down the wall.

Measurements of the reattachment length for the primary separation bubble, x_1 in Figure 2, just downstream of the step on the lower wall allowed the identification of the laminar ($Re < 1200$), transitional ($1200 < Re < 6600$) and turbulent ($Re > 6600$) regimes. The Reynolds number is evaluated with a reference velocity equal to two-thirds of the maximum velocity measured 10 mm upstream of the step and a reference length equal to twice the upstream channel height (i.e. the hydraulic diameter of the upstream channel). For the laminar regime the separation length increases non-linearly with the Reynolds number. The transitional flow regime is characterized by a sharp initial decrease in the reattachment length, followed by a continued gradual but irregular decrease to a minimum at a Reynolds number of approximately 5500. Beyond $Re = 6600$ the reattachment length ceases to be a function of the Reynolds number. An additional separation bubble was measured along the floor of the channel downstream of the primary separation, x_2 and x_3 in Figure 2. This secondary bubble disappears above a Reynolds number of 2300. A secondary separation region was also observed along the upper wall downstream of the step, x_4 and x_5 in Figure 2. It develops in the laminar regime (for $Re > 400$) and remains throughout the transition regime. The length of this upper separation bubble initially increases with increasing Reynolds number and then gradually decreases until it disappears above a Reynolds number of approximately 6600.

To determine the two-dimensionality of the flow, spanwise velocity profiles at various constant elevations were measured at selected Reynolds numbers. At Reynolds numbers smaller than 400 the

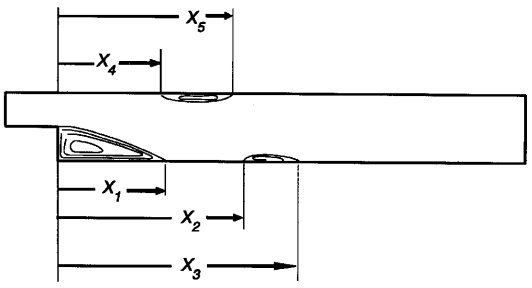

Figure 2. Separation regions identified by Armaly *et al.*[1]

flow was predominantly two-dimensional. Within the Reynolds number range of $400 < Re < 6600$ the flow downstream, and in the immediate vicinity of the step, was found to be three-dimensional. Armaly *et al.*[1] also noted that 'within and around the transition flow regime longitudinal vortices develop and destroy the two-dimensional character of the flow'. These vortices were shown to begin to develop in the laminar region at $Re \approx 800$.

2. COMPUTATIONAL EXPERIMENTS

2.1. Conservation law system

The conservation law system employed in this study consists of the physical principles of conservation of mass and momentum for a viscous isothermal fluid. Applying the incompressibility condition (constant density), the non-dimensional divergence form of the equation set representing this Navier–Stokes conservation law system is

$$\frac{\partial u_i}{\partial x_i} = 0 \quad \text{in } \Omega \subset \mathbb{R}^3, \tag{1}$$

$$\frac{\partial u_i}{\partial t} + \frac{\partial}{\partial x_j}\left[u_i u_j - \frac{1}{Re}\left(\frac{\partial u_i}{\partial x_j} + \frac{\partial u_j}{\partial x_i}\right) + P\delta_{ij}\right] = 0 \quad \text{in } \Omega \subset \mathbb{R}^3, \tag{2}$$

where, and throughout this paper, repeated italic indices imply summation over the dimension of the domain Ω. The requirement in (1) for a divergence-free or solenoidal velocity field represents a differential constraint on all admissible solutions to the momentum equations. In (1) and (2), $u_i(x_j, t)$ is the velocity vector resolution of the flow, t is time, $P(x_j, t)$ is the kinematic pressure (pressure divided by the constant density ρ), δ_{ij} is the Kronecker delta and Re is the Reynolds number. With superscript '*' indicating a dimensional state variable and subscript 'ref' denoting suitable dimensional reference scales, the scaling rules used to non-dimensionalize (1) and (2) are

$$u_i \equiv \frac{u_i^*}{U_{\text{ref}}}, \qquad x_j \equiv \frac{x_j^*}{L_{\text{ref}}}, \qquad t \equiv \frac{t^*}{L_{\text{ref}}/U_{\text{ref}}}, \qquad P \equiv \frac{P^*}{U_{\text{ref}}^2}, \qquad Re \equiv \frac{U_{\text{ref}} L_{\text{ref}}}{\nu},$$

where ν is the kinematic viscosity (assumed constant). The Navier–Stokes conservation law system is defined in the domain Ω with boundary closure $\partial\Omega = \Gamma_1 \oplus \Gamma_2 \oplus \ldots \oplus \Gamma_i$, where the Γ_i comprise disjoint boundary segments. Closure is complete upon definition of well-posed initial and boundary conditions.

2.2. Finite element weak statement CFD algorithm

A newly verified incompressible Navier–Stokes algorithm called the continuity constraint method (CCM) was used to discretely enforce the continuity differential constraint (1) while solving the momentum equations.[17,18] The CCM theory is implemented by a finite element spatial semidiscretization of a Galerkin weak statement in concert with a θ-implicit time integration scheme, a consistent mass matrix and equal-order interpolation (i.e. the finite element equivalent of a non-staggered mesh) of all state variable members. Iterative cycling within a time step with the CCM constraint function provides an approximate (and measurable) enforcement of conservation of mass. Once a converged solenoidal velocity field is obtained, the determination of the (genuine) kinematic pressure employs a pressure Poisson weak statement equation.[19]

The CCM finite element implementation is intrinsically devoid of artificial diffusion. Control of discretization-induced dispersion error is maintained in the CCM construction via a Taylor weak

statement (TWS) extension of the Galerkin weak statement formulation for the momentum equations. The TWS expression was derived by Noronha and Baker[20] to be

$$-\beta \frac{h^e}{|\mathbf{u}|_e} \frac{\partial}{\partial x_j} \left(u_j u_k \frac{\partial u_i}{\partial x_k} + u_i u_k \frac{\partial u_j}{\partial x_k} \right) \tag{3}$$

and is added to the ith momentum equation. Here $\beta \geqslant 0$ is the user-selectable TWS dissipation scale factor, h_e is an element-based mesh measure with the dimension of length and $|\bar{\mathbf{u}}|_e$ is an element-based reference speed.

A generalized conjugate gradient technique, called the restarted generalized minimal residual (GMRES(m)) iterative method[21] with diagonal scaling as a preconditioner, was used to solve the sequence of non-symmetric sparse linear algebra problems produced by the selected quasi-Newton linearization of the discretized weak statements for the momentum equation. A restart value of $m = 10$ (where m is the selected dimension of the Krylov subspace) was found to provide an acceptable compromise between CPU work and core memory requirements. For the symmetric positive definite matrix statements produced for the Poisson equations for pressure and continuity constraint function, an incomplete Cholesky preconditioned conjugate gradient iterative solver was used.[22] Details of this CFD methodology are presented by Williams and Baker,[18] Baker *et al.*[23] and Williams *et al.*[24] and summarized in the Appendix to this paper.

3. RESULTS AND DISCUSSION

Two- and three-dimensional models simulating the experiments of Armaly *et al.*[1] were developed for the current study. The two-dimensional model, Figure 3, used an $M = 4 \times 11 \times 1$ discretization upstream of the step and $M = 87 \times 20 \times 1$ downstream of the mesh, where all velocities in the z-coordinate direction are set to zero. Exploiting the experimentally verified symmetry of the flow field, the three-dimensional model, Figure 4, employed a central vertical symmetry plane with a mesh discretization of $M = 4 \times 11 \times 24$ upstream and $M = 87 \times 20 \times 24$ downstream of the step plane. The upstream and downstream, channels are approximately one and 30 step heights long respectively.

The final meshes for the two- and three-dimensional models resulted from a mesh refinement study that investigated the sensitivity of the solutions to (a) channel lengths upstream and downstream of the step and (b) the mesh refinement and grading near all walls, the step plane, regions of separation and the approach to the outflow plane. Seven stages of mesh refinement were investigated for the three-dimensional model, starting with approximately 20,000 nodes and progressing to the final mesh of 47,300 nodes. Using an approach length of 10 step heights, the initial two-dimensional results indicated that a fully developed velocity profile was well established within one step height from the inlet plane, allowing the shortening of the approach channel. The two- and three-dimensional studies also showed that adequate mesh grading was necessary both upstream and downstream of the step

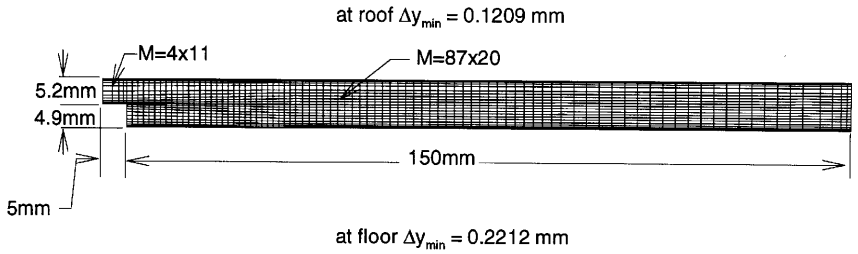

Figure 3. Mesh for two-dimensional model, $M = 4 \times 11 \times 1$ and $87 \times 20 \times 1$

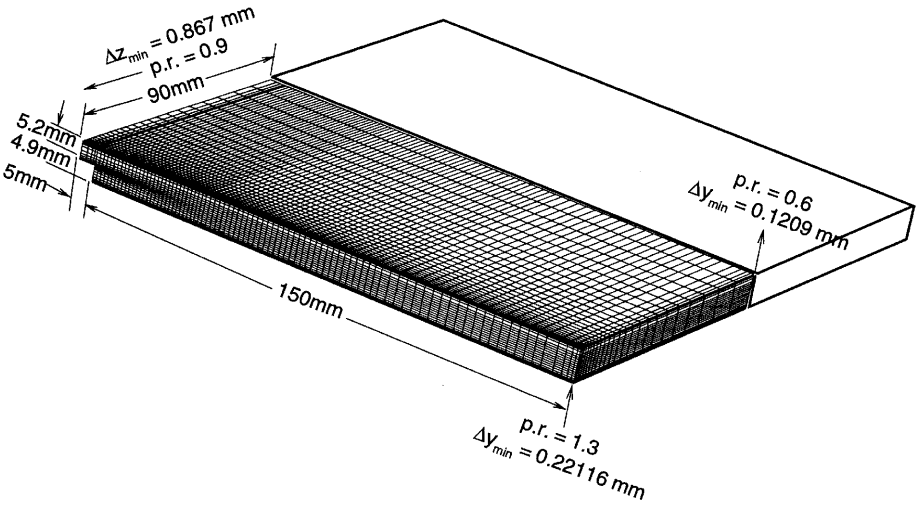

Figure 4. Mesh for three-dimensional model, $M = 4 \times 11 \times 24$ and $87 \times 20 \times 24$

plane. Grading along the upper wall was critical in the three-dimensional model for resolving the thin secondary separation region, and the solution became unstable if the mesh was inadequately graded near the outflow plane.

The velocity boundary conditions for both models included no-slip conditions at all impermeable walls, a prescribed fully developed laminar velocity profile at the inflow plane, a tangency condition on the symmetry plane and a zero-traction Neumann condition for the outflow plane as described by Williams.[17] At the inflow plane the two-dimensional model used the standard parabolic velocity profile and the three-dimensional model used the fully developed laminar solution for a duct with a rectangular cross-sectional area.[25] The pressure and the continuity constraint function Φ were both set to zero across the outflow plane. Except for the symmetry plane, the boundary condition for the constraint function was homogeneous Neumann. To maintain a free-slip condition for the symmetry plane, a non-homogeneous Neumann boundary condition for Φ is calculated as the solution evolves. The pressure boundary condition was homogeneous Neumann across the symmetry plane and non-homogeneous Neumann for the inflow and no-slip boundaries. For $Re = 100$ the initial conditions for the velocity field were a fully developed profile filling the upstream and downstream channels, where the downstream channel profile was scaled from the upstream profile by the cross-sectional area ratio (upstream to downstream) to provide a nominal conservation of mass at $t = 0{\cdot}0$. The initial pressure field was calculated by the pressure Poisson equation using the initial velocity data. For subsequent higher *Re* the converged solution from the previous lower *Re* was used as an initial condition. For both the two- and three-dimensional simulations, laminar steady state solutions were obtained for $100 \leqslant Re \leqslant 800$.

Preliminary results for the three-dimensional model indicated an instability in the computed velocity distribution at the step plane that did not respond to remeshing. It was postulated that the source of the instability was round-off error, produced by the significant difference in magnitude of the three velocity components. The problem was eliminated by rotating the computational co-ordinate system, relative to the 'laboratory' reference frame, through two successive Euler angles. The first transformation was $+45^\circ$ rotation about the z-co-ordinate axis, producing an (x', y', z')co-ordinate triad, and the second transformation involved a $+45^\circ$ rotation about the y'-co-ordinate axis to produce (x'', y'', z'') where all computations were performed. In the new reference frame, all three

velocity components were of the same order of magnitude as measured by their respective energy seminorms, defined by

$$\|q\|_E^2 \equiv \frac{1}{C}\sum_e \left(\int_{\Omega_e} \frac{\partial q}{\partial x_j}\frac{\partial q}{\partial x_j}\, d\Omega \right), \tag{4}$$

where q represents any state variable and C is a normalizing constant.

A number of researchers have used the experimental data of Armaly *et al.*[1] for computational validation studies.[1,11,16,26–36] A representative sampling from the literature is presented in Table I. The CFD formulations include a range of algorithms, such as the finite difference MAC, finite volume SIMPLE, finite element penalty, pseudospectral and finite element least squares formulations. The Reynolds numbers cited in the far right column are calculated using a consistent reference velocity and length scale. As described by Armaly *et al.*,[1] the reference velocity is the average bulk velocity in the upstream channel (defined as two-thirds of the maximum axial velocity measured 10 mm before the step plane) and the reference length is the hydraulic diameter of the upstream channel (defined as the twice the upstream channel height).

Primary reattachment lengths, normalized by the step height S, are plotted as a function of the Reynolds number in Figure 5. The two-dimensional computational data reported by various researchers show good agreement with the experimental values up to $Re \approx 400$. Above $Re = 400$ the computational results diverge, as expected, from the experimental data of Armaly *et al.*[1] (full line). It has been postulated that the reason the two-dimensional solutions cease to agree with the experimental reattachment data is the three-dimensionality of the flow.[16]

In Figure 6 the reattachment lengths of the primary separation region for these symmetry plane data are compared with the experimental data of Armaly *et al.*[1] and the three-dimensional computational results of Ku *et al.*[30] and Jiang *et al.*[36] The present three-dimensional results show excellent agreement with the primary reattachment data of Armaly *et al.*,[1] especially above the Reynolds number at which the two-dimensional solutions begin to diverge.

Table I. Computational studies of backward-facing step

Researcher(s)	Method/code	Dim.	Mesh	Reynolds number
Armaly *et al.*[1]	SIMPLE/TEACH	2D	45 × 45	⩽ 1250
Kim and Moin[26]	Chorin's projection method	2D	101 × 101	100–800
Durst and Pereira[27]	SIMPLE with QUICK	2D	85 × 65	10–648
Guj and Stella[28]	Vorticity–velocity	2D	101 × 40	80–800
Sohn[29]	Penalty/FIDAP	2D	61 × 33	100–800
Ku *et al.*[30]	Pseudospectral matrix element (PSME)	2D	297 × 33	75–450
Ghia *et al.*[16]	Vorticity–streamfunction	2D	195 × 33	300–1200
Thangam and Knight[31]	SIMPLE	2D	120 × 61	33·3–600
Gartling[11]	Penalty/NACHOS II & FIDAP	2D	800 × 40	800
Ikohagi and Shin[32]	SMAC	2D	70 × 21	100–800
Cabuk *et al.*[33]	Preconditioned pseudocompressibility	2D	121 × 21	100–600
Ku *et al.*[30]	Pseudospectral matrix element (PSME)	3D	42 × 36 × 48	75–450
Ikohagi *et al.*[34]	SMAC	3D	75 × 35 × 31	1000
Steinthorsson *et al.*[35]	Advection upwind splitting method/TRAF3D	3D	161 × 65 × 30	100–389
Jiang *et al.*[36]	Least squares finite element	3D	82 × 32 × 20	100–800

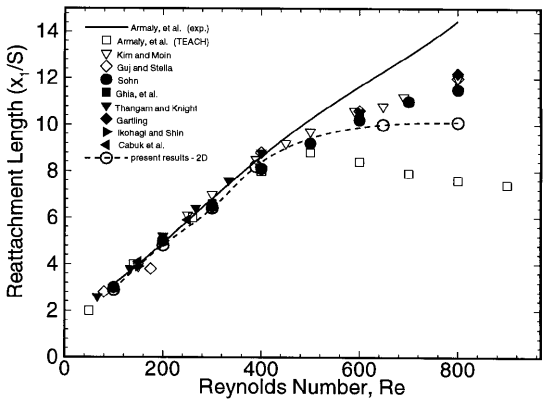

Figure 5. Primary reattachment length versus *Re*, two-dimensional solutions

To demonstrate the two- and three-dimensional character of the flow below and above $Re = 400$ respectively, Armaly *et al.*[1] reported measured spanwise velocity profiles for $Re = 397$ and 648. For $Re = 397$ the spanwise scans were taken at an elevation 7·5 mm above the floor of the downstream channel, Figure 7(a). The present CCM results from three *x*-stations, Figure 8(a)–8(c), confirm that the flow is essentially two-dimensional except directly adjacent to the sidewall. At $x/S = 6{\cdot}22$, which is upstream of the measured primary reattachment point, the two-dimensional character of the flow field is fully confirmed by the present results over a vertical span. However, the magnitude of the computed axial velocity exceeds the experimental value at $y = 7{\cdot}5$ mm. The low level of the experimental velocity is predicted by the CCM to occur 2 mm above the 7·5 mm elevation as graphed in Figure 8(a).

The CCM computational results are in very good agreement with the experimental axial profile at $x/S = 14{\cdot}3$, downstream of the reattachment of the primary separation. Further downstream at $x/S = 18{\cdot}8$ the experimental profile shows a significant increase in average velocity, while the computational profile indicates a slight decrease (compare 8(b) and 8(c)). At all *x*-stations plotted, the three-dimensional nature of the flow near the sidewall is substantially resolved in the present results, which was apparently beyond the detection range of the experimental configuration. As will be

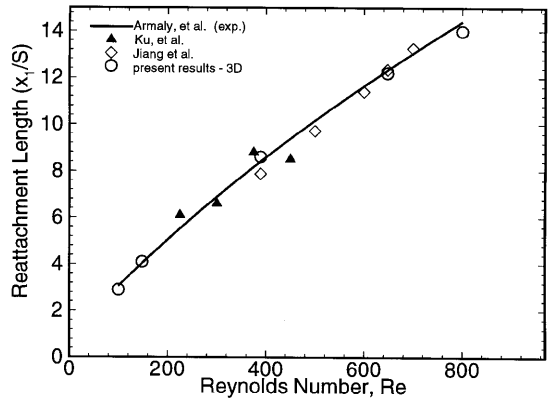

Figure 6. Primary reattachment points on three-dimensional symmetry plane verus *Re*

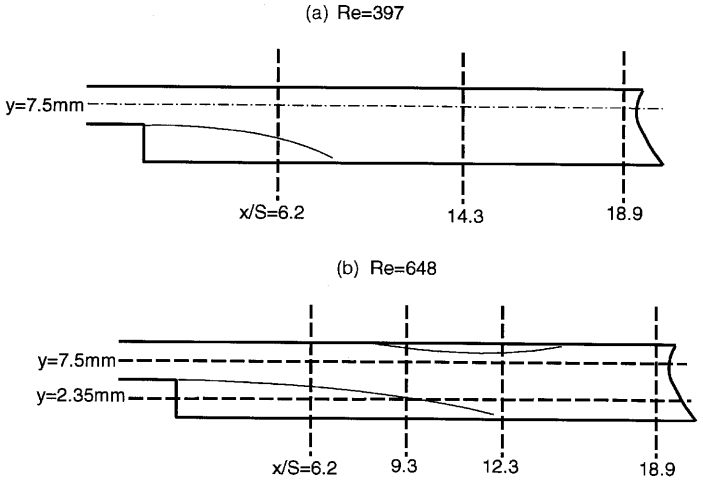

Figure 7. Locations of transverse planes for spanwise axial velocity profiles

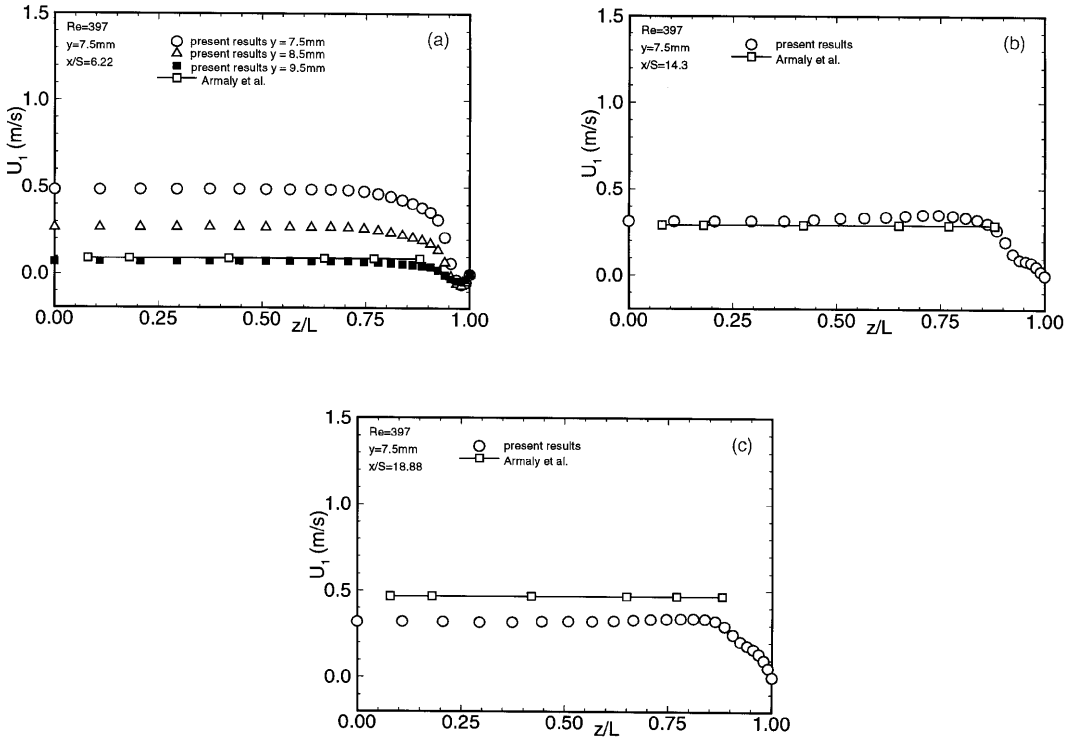

Figure 8. Comparison of spanwise velocity distributions, $Re = 397$

shown, these three-dimensional structures near the sidewall have a dominating influence on the central flow field at higher Reynolds numbers.

For $Re = 648$, experimental spanwise scans were taken at four x-stations and for two elevations, Figure 7(b). The data of these scans are graphed and linearly interpolated in Figure 9 for $y = 7{\cdot}5$ mm and in Figure 10 for $y = 2{\cdot}35$ mm. Armaly *et al.* report that at this Reynolds number the flow is fully three-dimensional as confirmed by the variation in axial velocity across the lateral span of the flow field. In general, very good agreement between the present CFD simulation and the experimental data at all x-stations and at both elevations is verified. The persistent flow reversals near the sidewall, missed in the experiments owing to their limited range, are an indication of significant flow separation, hence reversal, all along the duct sidewall for $x/S \leqslant 18$.

The data of Armaly *et al.* also included axial velocity profiles at the midplane of the channel for a range of Reynolds numbers at different x/S locations. Visual comparisons of the experimental velocity data for $Re = 389$ (Figure 16 of Reference 1) with the present results in Figure 11(a) showed good agreement. Velocity profile data from the present results for $Re = 397$, 648 and 800 are also presented in Figures 11(b)–11(d) respectively. The elevation locations for the spanwise axial velocity sans are denoted by the circles in Figures 11(b) and 11(c).

Contours of negatively directed axial velocity are presented in Figures 12–14 to aid in visual interpretation of the primary and secondary separation regions on the lower 'floor', upper 'roof' and sidewall of the channel. The graphed floor, roof and sidewall CFD data are those on the first interior plane of nodes, adjacent to the corresponding no-slip boundaries. In these figures the roof has been opened like a book about the duct roof centroidal x-axis for visualization. At $Re = 389$, Figure 12, the flow is confirmed nominally two-dimensional over approximately the central two-thirds of the

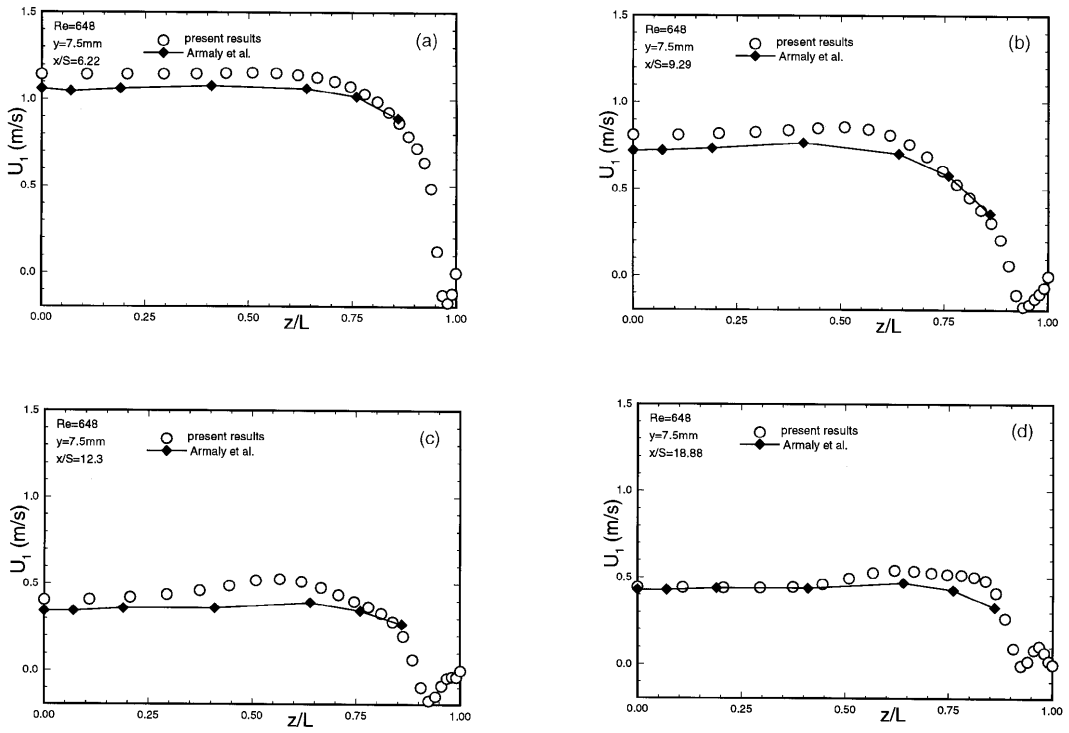

Figure 9. Comparison of CFD and experimental spanwise velocity profiles, $y = 7{\cdot}5$ mm $Re = 648$

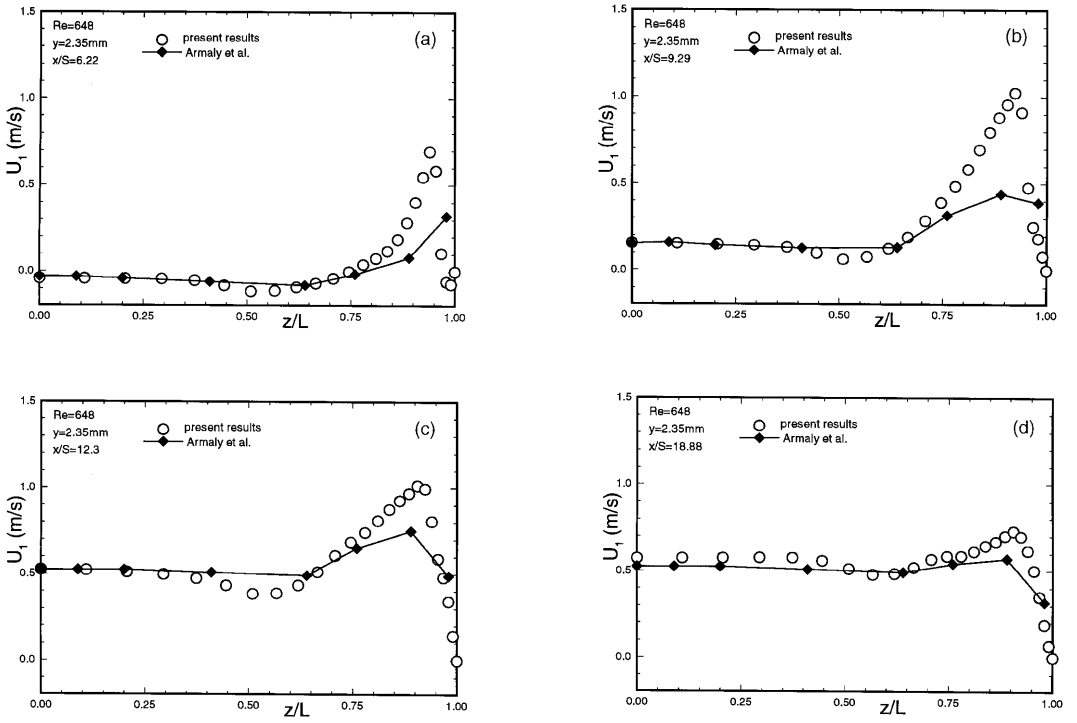

Figure 10. Comparison of CFD and experimental spanwise velocity profiles, $y = 2{\cdot}35$ mm $Re = 648$

channel span. No secondary region has yet developed on the roof near the symmetry plane; however, a significant three-dimensional separation region exists along the sidewall axial corners, extending well downstream of the reattachment line for the primary separation region. In the three-dimensional numerical study of this same step geometry by Steinthorsson *et al.*[35] a large region of reversed flow in the immediate vicinity of the sidewall was also observed for $Re = 389$; however, results for $Re > 389$ were not reported.

At $Re = 648$ and 800, Figures 13 and 14 respectively, the primary separation bubble continues to grow, as does the penetration of the sidewall corner separation regions axially and out into the main flow field. The secondary separation bubble on the roof near the symmetry plane is very thin (approximately 1 mm) and does not connect with the sidewall separation region for $Re \leqslant 800$.

Another enhancement to improved visualization of the flow field is the computation of 'oilflow' streaklines, as calculated from the projection of the velocity field onto horizontal planes near the floor and the roof. For $Re = 800$ the full lines with arrows, Figure 15, are such streaklines demonstrating the significant three-dimensional flow character around and within the primary and secondary separation regions. The pronounced vertical axis vortex in the flow near the roof, Figure 15(b), is very shallow (as will be examined further using a Lagrangian particle track in this region).

Flow field enlargements near the sidewall at $Re = 800$ are projected in Figure 16 onto transverse planes, located at $x_1/S = 7{\cdot}72$ and $18{\cdot}37$ step heights from the step. These transverse projections clearly show the strong three-dimensionality of the flow involving a wall jet at the step and complex vortex structures that extend well beyond the region of reverse flow, in the upper and lower corners of the channel, and into the central flow field. (The perspective graphs are included to provide a sense of the location of the transverse planes.) The full curves separate the regions of positive and negative

(a) Re = 389

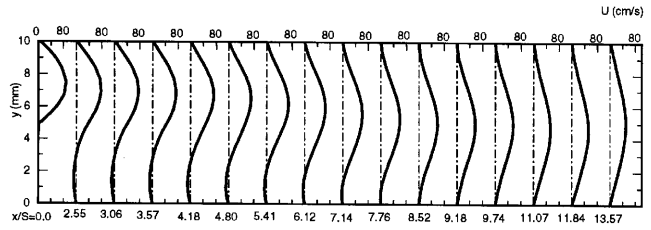

(b) Re = 397

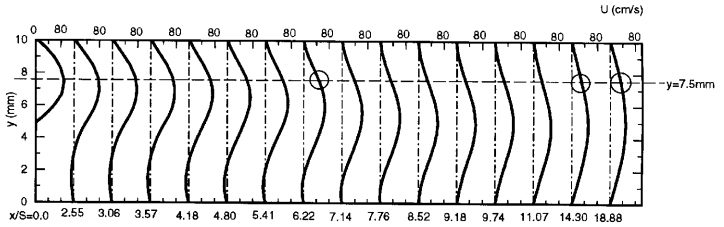

(c) Re = 648

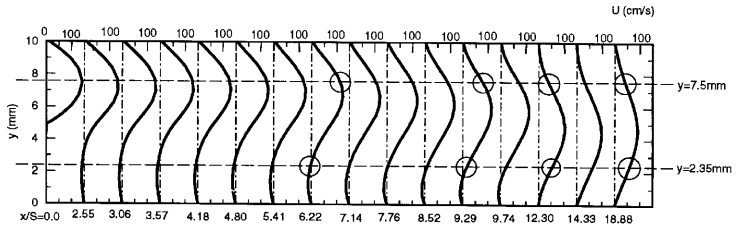

(d) Re = 800

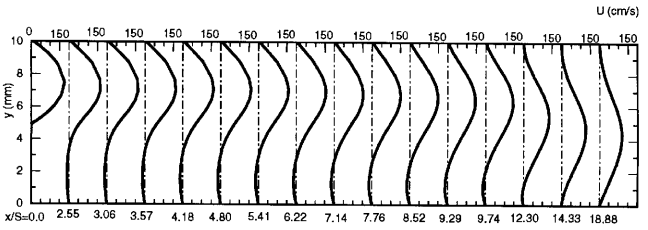

Figure 11. Present results of axial velocity profiles at symmetry plane ($z = 0$) at different x/S locations

axial velocity ($\pm u_1$) in each graph. For $x_1/S = 18{\cdot}37$ there is evidence of a developing longitudinal vortex as discussed by Armaly *et al.* for $Re \approx 800$.

Lagrangian particle tracks were calculated from steady state velocity vector solutions using a modified Euler integration scheme suggested by Mallinson and de Vahl Davis.[37] For a particle release point in the step plane of (5, 5·1, 89) which is 1 mm away from the sidewall and 0·2 mm above the

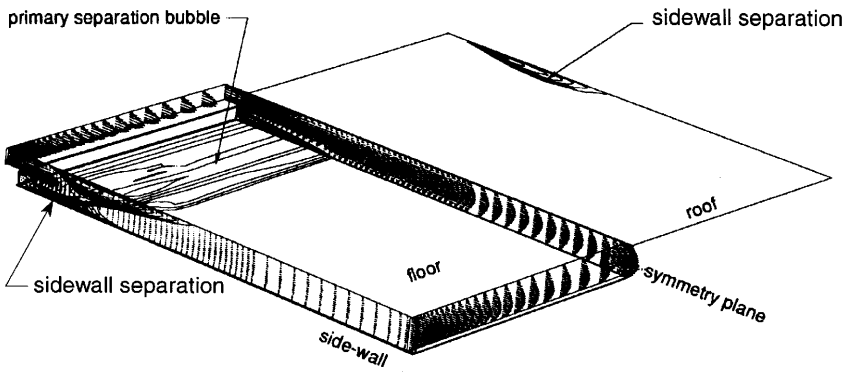

Figure 12. Separation region 'footprints', $Re = 389$

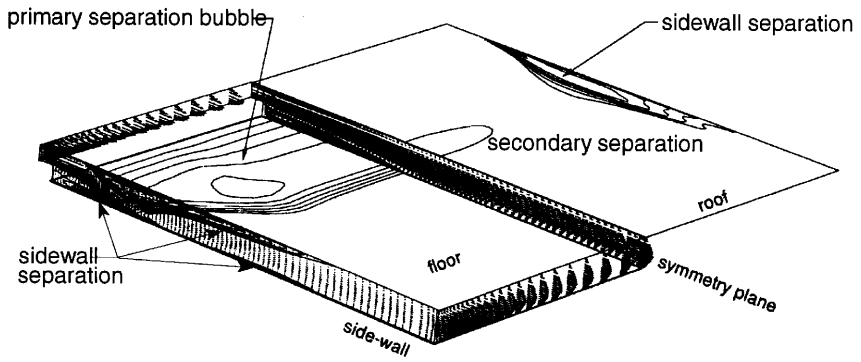

Figure 13. Separation region 'footprints', $Re = 648$

top of the step, the tracks for $Re = 389$, 648 and 800 are shown in Figures 17–19 respectively. The diameter of the particle symbol (the 'bubble') is linearly related to its elevation above the channel floor, while the distance between each bubble represents a constant elapsed time interval. The three particle tracks within the primary separation region reveal the general shape of a vortex with its axis parallel to the channel floor and normal to the mainstream flow direction. The particles move along a spiral path towards the symmetry plane where they are eventually caught up in a predominantly two-

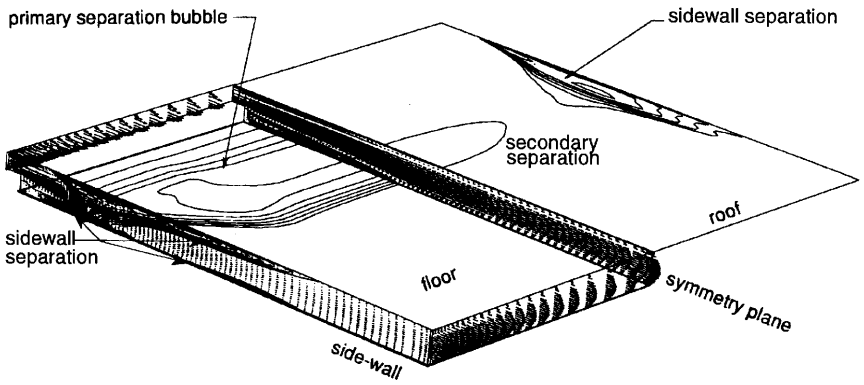

Figure 14. Separation region 'footprints', $Re = 800$

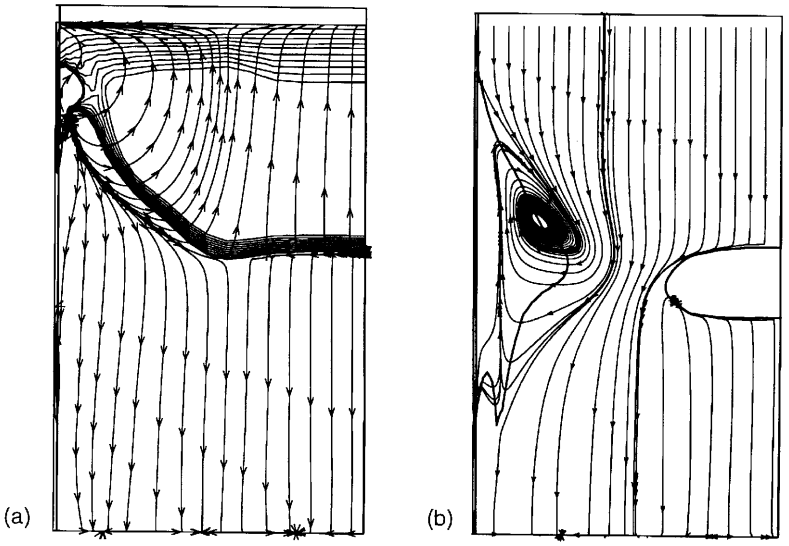

Figure 15. Oil flow streaklines at $Re = 800$ on horizontal planes: (a) flow near floor; (b) flow near roof

dimensional recirculating flow and then exit the separation bubble into the mainstream flow. With increasing Reynolds number the extent of the two-dimensional flow region decreases and the penetration of the three-dimensional vortex moves closer to the symmetry plane. In Figure 20 the particle release point is near the vertical axis vortex shown in Figure 15(b). Note that the bubble diameter is generally uniform, confirming the shallowness of the vortex structure at this location, before it descends and moves downstream.

Ghia *et al.*[16] have suggested two possible mechanisms for what they termed an 'abrupt change' in flow structure from two- to three-dimensional flow when the secondary separation bubble first appears on the upper wall at $Re \approx 400$. They note that two-dimensional boundary layer flows, subject to a locally destabilizing concave curvature of the boundary, are susceptible to a Taylor–Görtler vortex instability. Spanwise-periodic counter-rotating pairs of vortices with axes aligned with the main flow direction are formed as a result of this instability. It has been suggested that such a vortex instability could be a common phenomenon near two-dimensional separation points. Ghia *et al.*[16] postulate that the appearance of the secondary separation bubble on the upper wall provides the necessary conditions for the formation of Taylor–Görtler vortices, and they propose 'that the additional mixing which would accompany a developing Taylor–Görtler instability would tend to delay the upper wall separation; thus causing the secondary separation point, x_4, to occur farther downstream than would be predicted on the basis of a strictly two-dimensional analysis'. The delay of the detachment of the secondary separation decreases its blocking effect and allows the development of a longer reattachment length for the primary separation bubble than would be predicted in the absence of this three-dimensional disturbance.

The alternative mechanism suggested by Ghia *et al.*[16] involves the growth and interaction of the boundary layers on the sidewalls of the test section. They rejected this mechanism based upon their assumption that the effect would tend to decrease with increasing Reynolds number owing to a thinning of the sidewall boundary layers.

The present results support the contention that the formation and structure of the upper separation region are a critical element in explaining the divergence of two-dimensional simulations from the experimentally observed primary reattachment lengths. Comparison of the two- and three-

(a) $x/S = 7.72$

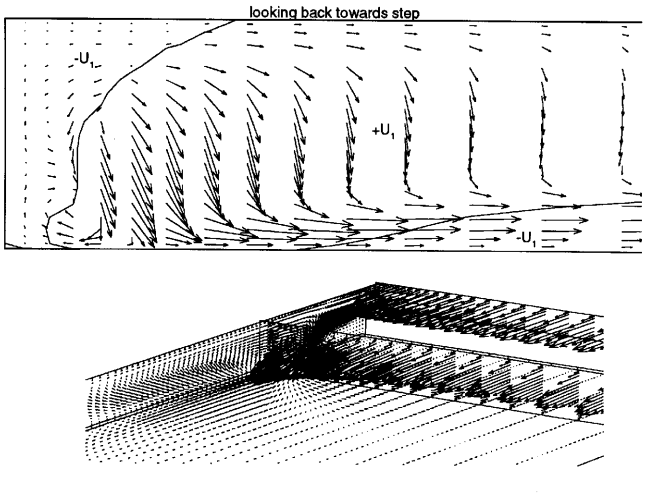

(b) $x/S = 18.37$

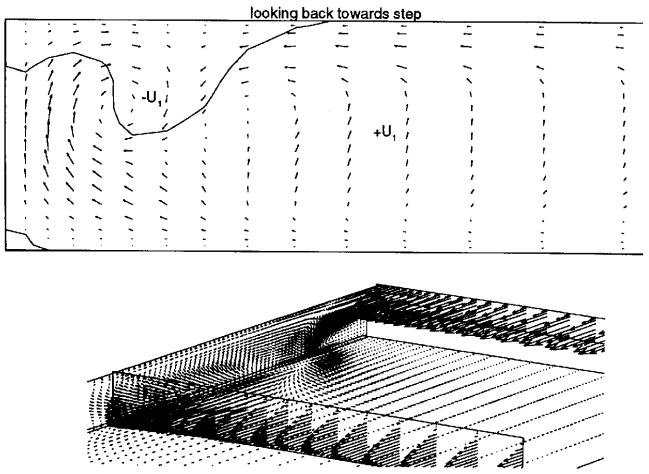

Figure 16. Flow field near sidewall projected onto transverse planes, $Re = 800$

dimensional results shows that a much thicker separation bubble is formed in the two-dimensional simulation which, once established, produces a relatively stationary blockage of the channel. This blocking effect serves to prevent the growth of the primary reattachment length with increasing Reynolds number.

Armaly *et al.*[1] present the spanwise velocity profiles shown in Figures 8–10 as evidence for their contention that the flow is two-dimensional for $Re < 400$ and three-dimensional for $Re > 400$. There is generally good agreement between the present results and their experiments for $Re = 397$ and excellent agreement for $Re = 648$. The present computational results, however, reveal details of the flow structure, unavailable to Armaly *et al.*,[1] which suggest a third mechanism for the development of strongly three-dimensional flow with increasing Reynolds number.

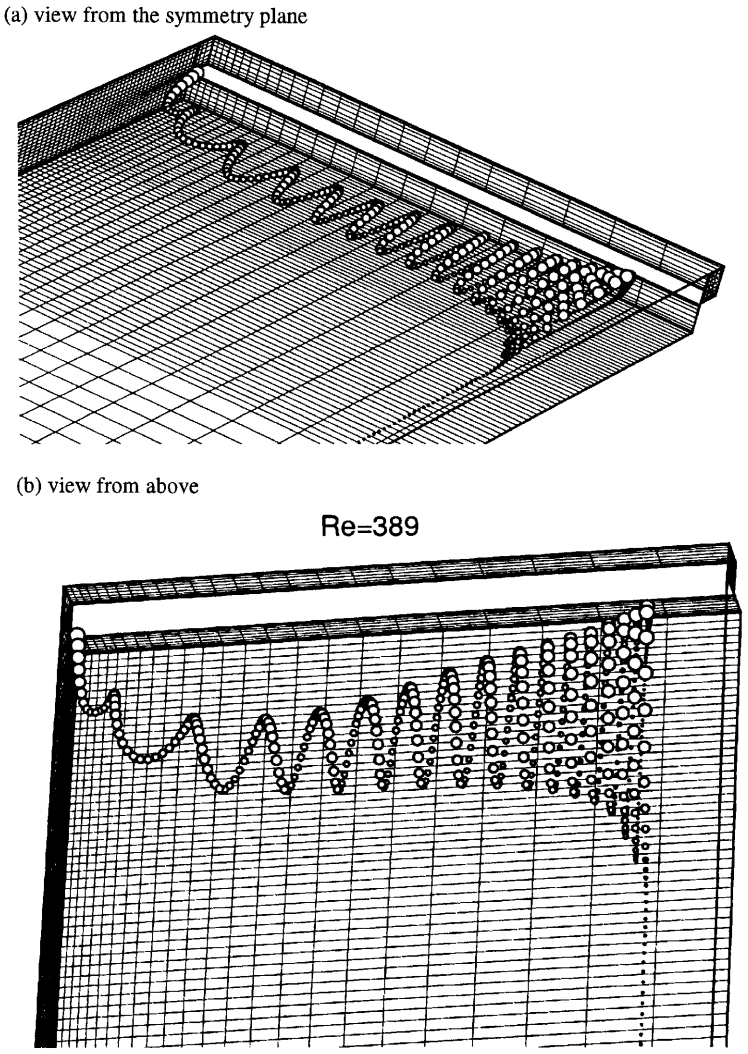

Figure 17. Lagrangian particle track for $Re = 389$

A wall jet, attached to the sidewall as shown in Figure 16, forms at the step plane and grows in strength with increasing Reynolds number. Observed at the lowest Reynolds number simulated ($Re = 100$), this wall jet, interacting with separation regions along the upper and lower corners of the sidewall, is the source of three-dimensional vortices in the vicinity of the sidewall which penetrate the central flow stream within the primary separation region. The particle tracks in Figures 17–20 reveal a fascinating picture of very complex three-dimensional flow structures. Even at $Re = 389$ the tracking particle, released at the source of the wall jet in Figure 17, shows a spiralling three-dimensional path from the sidewall to the central symmetry plane. Nearing the symmetry plane, the particle joins the essentially two-dimensional primary separation region. As the Reynolds number increases, the wall jet strengthens and the point at which the tracking particle is caught up by the central separation region moves closer to the symmetry plane, Figures 18 and 19. Rather than thinning, the separation region along the sidewall continues to develop with increasing Reynolds

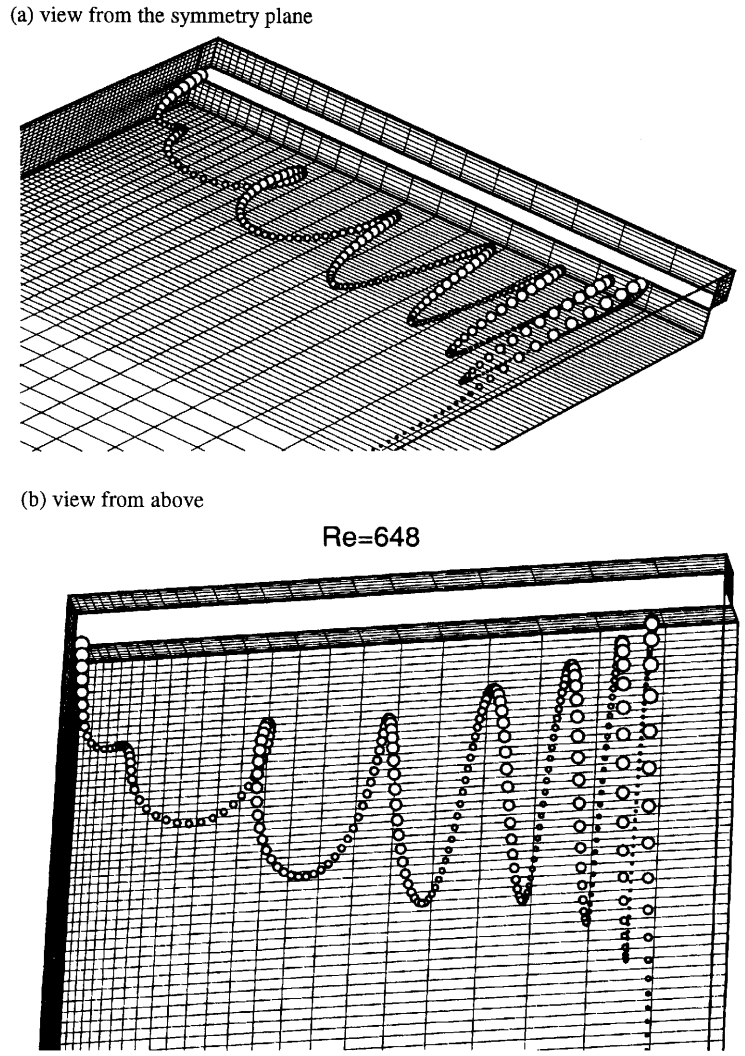

Figure 18. Lagrangian particle track for $Re = 648$

number. Complex three-dimensional vortices can be observed along the sidewall, Figure 16, and the roof, Figure 20. In summary, the present results show that the transition from two- to three-dimensional flow is not an abrupt change but rather a continuous penetration of three-dimensional flow, fed by a wall jet, from the sidewall to the central symmetry plane.

4. CONCLUSIONS

A numerical investigation of laminar flow over a three-dimensional backward-facing step has been carried out. Comparisons with the detailed experimental data of Armaly *et al.*[1] served to validate the numerical results. The continuity constraint method, implemented via a finite element semidiscretized Taylor weak statement, was employed to solve the unsteady three-dimensional Navier–Stokes equations for incompressible laminar isothermal flow. Two-dimensional simulations of this step

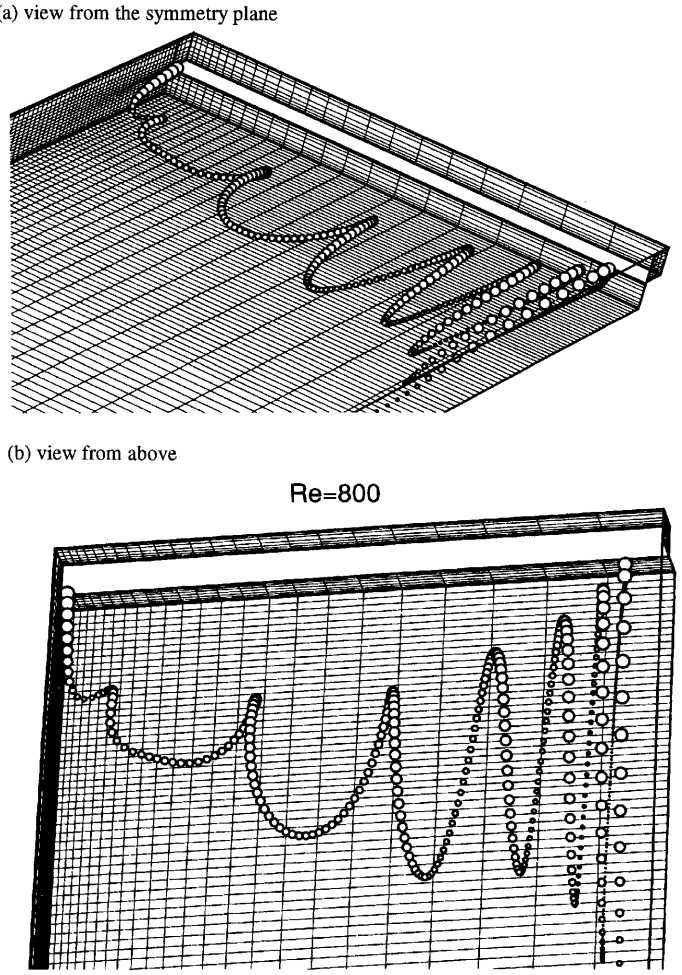

Figure 19. Lagrangian particle track for $Re = 800$

geometry have typically underestimated the experimentally determined extent of the primary separation region for $Re > 400$. It has been postulated that this disagreement between physical and computational experiments is due to the onset of three-dimensional flow near $Re \approx 400$. A full three-dimensional simulation of Armaly *et al.*'s step geometry for $100 \leqslant Re \leqslant 800$ correctly predicts the primary reattachment lengths, thus confirming the influence of three-dimensionality. Previous numerical studies[22,25] have presented possible instability modes which could induce a sudden onset of three-dimensional flow at certain critical Reynolds numbers.

The current investigation demonstrates the clear influence of the sidewall in generating three-dimensional effects for the geometry of Armaly *et al.*'s experiment. Various flow visualization techniques demonstrate the rich character of the sidewall-induced three-dimensional vortices in the primary separation region immediately downstream of the step. The complex interaction of a wall jet, located at the step plane near the sidewall, with the mainstream flow reveals a mechanism for the increasing penetration (with increasing Reynolds number) of three-dimensional flow structures into a

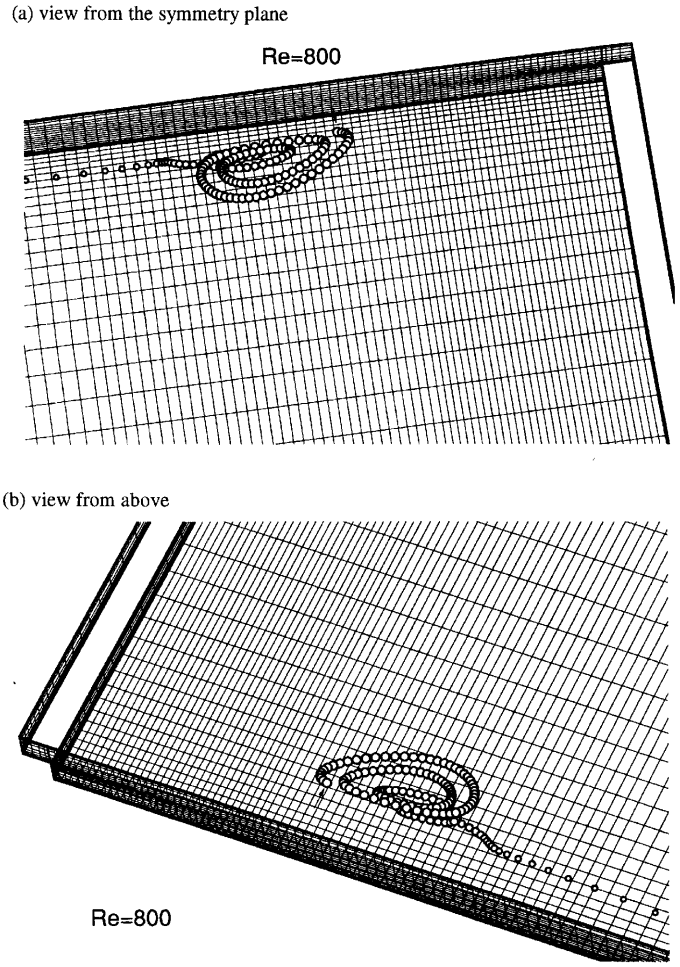

Figure 20. Lagrangian particle track, release point near vertical axis vortex structure at roof, $Re = 800$

region of essentially two-dimensional flow near the spanwise midplane of the channel. The character and extent of the sidewall flow have been established for $100 \leqslant Re \leqslant 800$.

APPENDIX: CCM OVERVIEW

A new primitive variable finite element CFD algorithm, the *continuity constraint method* (CCM), has been developed to produce approximate solutions for the unsteady Navier–Stokes equations in three dimensions. Falling in the general class of *pressure relaxation* algorithms, the new method has its origins in the finite difference SMAC method,[38] the finite element velocity correction method[39] and developments in incompressible algorithm research at the University of Tennessee's CFD Laboratory.[17,18]

Recognition of the dual role of the pressure, both as an enforcer of the continuity constraint and as a force in the mechanical balance law for the conservation of linear momentum,[40] has been a guiding principle in the algorithm's development. An implicit time integration with iterative cycling within

the time step allows the two roles for the pressure to be completely separated. Specifically, a mass-conserving potential function is used to enforce continuity while the genuine pressure, as induced by a solenoidal velocity field, is calculated with well-posed and physically motivated boundary conditions by the pressure Poisson equation. This separation of tasks produces a clear view of the individual and totally distinct boundary conditions required for the continuity constraint function and the pressure.

Additionally, the CCM employs a θ-implicit time integration scheme, a consistent mass matrix, an optional Taylor weak statement (TWS) formulation for dispersion error control and equal-order interpolation of all state variables. Implicit time integration allows larger stable time steps compared with explicit schemes. A consistent full mass matrix, as opposed to the 'lumped' mass matrix commonly used in explicit methods, exploits the cross-coupling in the inertial terms of the momentum and energy equations produced by the finite element semi-discretization. The TWS theory has been employed by Baker and Kim[41] to identify a multidimensional tensorial mechanism for hyperbolic conservation law systems. The derived stability formulation was later verified as highly effective in control of third-order dispersive error mechanisms.[42] Equal-order interpolation of the velocity, pressure and temperature state variables with trilinear and bilinear (for boundary condition surface integrals) basis functions produces a continuous and more accurate pressure solution.

For an implicit time integration of the momentum equations an iterative cycle within the time step is required. During these outer iterations the CCM replaces the genuine pressure in the momentum equations with a continuity constraint state variable C^p_{n+1}, where the superscript p is an iteration index and $n+1$ is the current time station. The θ-implicit semidiscrete momentum equations therefore have the form

$$u_i|^p_{n+1} = u_i|_n - \theta\Delta t\left\{\frac{\partial(u_j u_i)}{\partial x_j} - \frac{\partial}{\partial x_j}\left[\frac{1}{Re}\left(\frac{\partial u_i}{\partial x_j}+\frac{\partial u_j}{\partial x_i}\right)\right] + \frac{\partial C}{\partial x_i}\right\}^p_{n+1} - (1-\theta)\Delta t\left\{\frac{\partial(u_j u_i)}{\partial x_j} - \frac{\partial}{\partial x_j}\left[\frac{1}{Re}\left(\frac{\partial u_i}{\partial x_j}+\frac{\partial u_j}{\partial x_i}\right)\right] + \frac{\partial P}{\partial x_i}\right\}_n, \tag{5}$$

where $0{\cdot}5 \leqslant \theta \leqslant 1{\cdot}0$ is an implicitness parameter and Δt is the discrete time step. When the genuine pressure P is required, it is assumed computable from the pressure Poisson equation, i.e.

$$\frac{\partial^2 P}{\partial x_i \partial x_i} + \frac{\partial u_j}{\partial x_i}\frac{\partial u_i}{\partial x_j} = 0, \tag{6}$$

for any $u_i|_{n+1}$, a converged, solenoidal velocity vector field. The genuine non-homogeneous Neumann boundary condition for (6) is

$$\frac{\partial P}{\partial n} = \frac{\partial}{\partial x_j}\left(\frac{1}{Re}\frac{\partial u_n}{\partial x_j}\right) - \frac{\partial u_n}{\partial t} - u_j\frac{\partial u_n}{\partial x_j} \quad \text{on } \Gamma_D, \tag{7}$$

where Γ_D is the union of all boundary segments where the velocities are fixed by Dirichlet data, e.g. walls and inflow planes.

The iterative cycle in the CCM requires the solution of a Poisson equation for a continuity constraint potential function Φ. This Poisson equation has the form

$$\left.\frac{\partial^2 \Phi}{\partial x_i \partial x_i}\right|^p = \left.\frac{\partial u_i}{\partial x_i}\right|^p_{n+1}. \tag{8}$$

The boundary conditions for Φ on Γ_D are homogeneous Neumann:

$$\left.\frac{\partial \Phi}{\partial n}\right|^{p+1} = 0 \quad \text{on } \Gamma_D. \tag{9}$$

The CCM iterative solution strategy is as follows.

Time step $n+1$

1. Initialize the constraint state variable by either $C_{n+1}^1 = C_n^{p+1}$ or $C_{n+1}^1 = P^n$.
2. Solve the momentum and energy equations implicitly for $\mathbf{u}^{*p}$.
3. Solve the Poisson equation for Φ^p.
4. Update the approximation for C_{n+1} by

$$C_{n+1}^{p+1} = C_{n+1}^1 + \frac{1}{\theta \Delta t} \sum_{k=1}^{p} \Phi^k.$$

5. Repeat steps 2–4 until

$$\|\Phi^p\|_E < \epsilon, \text{ convergence tolerance}.$$

6. Advance the time step; solve the genuine pressure Poisson equation for P^{n+1}.

Since equal-order interpolation of all state variables is employed, which is the finite element equivalent of using a non-staggered mesh, the div-stability condition is not satisfied by the CCM. As a result, there is a dominant dispersive error mode, *modulo* ∇^h, associated with Φ. One significant computational attribute of the genuine pressure Poisson solve in step 6 is that it prevents the dispersive error from polluting the velocity and temperature solutions. Step 6 also provides the means for establishing a basis (i.e. a continuous C_{n+1}^l based on the genuine pressure P^n) for an approximation of P^{n+1} during the iterative cycle. Experience with the CCM has shown that the pressure Poisson solve can be subcycled (e.g. solved every third, fourth or 40th time step) to improve computational efficiency.

Step 5 defines the *stopping test* for the outer iteration cycle in terms of the energy seminorm of Φ, defined as

$$\|\Phi^p\|_E \equiv \frac{1}{2} \int_\Omega \frac{\partial \Phi}{\partial x_j} \frac{\partial \Phi}{\partial x_j} \, \mathrm{d}\Omega|_{n+1}^p. \tag{10}$$

By the definition of Φ,

$$\left.\frac{\partial \Phi}{\partial x_i}\right|^{p+1} \equiv (u_i^* - u_i)|_{n+1}^p, \tag{11}$$

where $u_i^* - u_i$ is the divergence error in the currently computed flow field, this energy seminorm of Φ can be seen to be a measure of the kinetic energy of the error in the current approximation for $u_i|_{n+1}$.

The conservation law system constitutes a non-linear coupled set of initial value partial differential equations (PDEs) whose solutions are constrained by the incompressibility condition. These PDEs can be expressed in the general form

$$\mathscr{L}(q) = \frac{\partial q}{\partial t} + \frac{\partial}{\partial x_j}\left(f_j - f_j^{\mathrm{v}}\right) = 0 \quad \text{on } \Omega \subset \mathbb{R}^n, \quad t \geqslant t_0, \tag{12}$$

where $\mathscr{L}(q)$ is a differential equation system written on the state variable $q(x_j, t)$. The function f_j is called the *kinematic flux vector* and f_j^{v} is the *viscous flux vector*. For the Navier–Stokes equations in $\mathbb{R}^3$ and negligible viscous dissipation, q, f_j and f_j^{v} have the definitions

$$q \equiv \begin{Bmatrix} u_1 \\ u_2 \\ u_3 \end{Bmatrix}, \qquad f_j \equiv \begin{Bmatrix} u_j u_1 + P\delta_{1j} \\ u_j u_2 + P\delta_{2j} \\ u_j u_3 + P\delta_{3j} \end{Bmatrix}, \qquad f_j^{\mathrm{v}} \equiv \frac{1}{Re} \begin{Bmatrix} \partial u_1/\partial x_j \\ \partial u_2/\partial x_j \\ \partial u_3/\partial x_j \end{Bmatrix}. \tag{13}$$

The algorithm auxiliary quasi-linear Poisson PDEs have the general form

$$\mathscr{L}(q_\alpha) = \nabla^2 q_\alpha - s_\alpha(q) = 0 \quad \text{on } \Omega \subset \mathbb{R}^n, \quad t \geqslant t_0, \tag{14}$$

where

$$q_\alpha \equiv \begin{Bmatrix} \phi \\ P \end{Bmatrix}, \qquad s_\alpha \equiv \begin{Bmatrix} \nabla \cdot \mathbf{u}^* \\ -\nabla \cdot [\mathscr{L}(\mathbf{u}) - \nabla P] \end{Bmatrix}. \tag{15}$$

Proceeding to the discrete form of (12), the state variables q and q_α are replaced by a continuous approximation that assumes the separability of space and time; thus

$$q(x_j, t) \equiv q^N(x_j, t) \equiv \sum_{i=1}^{N} \Psi_i(x_j) Q_i(t), \tag{16}$$

where the function set $\Psi_i(x_j)$, called the approximation 'trial space', is user-selectable. The superscript N in (16) denotes *any* approximate solution produced via the inner product of the known trial function $\Psi_i(x_j)$ and the set of unknown coefficients $Q_i(t)$.

The *weak statement* is a continuum form of the *method of weighted residuals* for constraining the error in q^N. One seeks the vector function $u_i(x_j, t) \in H_0^1(\Omega)$ and the scalar functions $\phi(x_j, t) \in L_0^2(\Omega)$ and $P(x_j, t) \in L_0^2(\Omega)$ such that

$$\int_\Omega w(x_i, t) \mathscr{L}(q^N)\, \mathrm{d}\tau = 0 \quad \forall w \in H_0^1(\Omega), \tag{17}$$

where the velocity vector function u_i^N is also constrained to sit in Z, the space of weakly divergence-free functions. The requirement that (17) must hold for any test function $w(x_j, t) \in H_0^1$ is enforced by making the integral stationary with respect to any set of $W_i(t)$, where the interpolation of $w(x_j, t)$ is carried out by

$$w^M(x_j, t) \equiv \sum_{i=1}^{M} \Phi_i(x_j) W_i(t). \tag{18}$$

This extrenum is termed a 'weak statement' with the form

$$\begin{aligned} WS^N &\equiv \frac{\partial}{\partial W_i} \int_\Omega w^M(x_j, t) \mathscr{L}(q^N)\, \mathrm{d}\tau \quad \forall i, \\ &= \int_\Omega \Phi_i(x_j) \mathscr{L}(q^N)\, \mathrm{d}\tau = 0 \quad \text{for } 1 \leqslant i \leqslant M. \end{aligned} \tag{19}$$

The optimal choice for the test function set $\Phi_i(x_j)$, is that it be identical with the trial space $\Psi_i(x_j)$. This decision yields a *Galerkin weak statement*

$$GWS^N \equiv \int_\Omega \Psi_i(x_j) \mathscr{L}(q^N)\, \mathrm{d}\tau = 0 \quad \text{for} 1 \leqslant i \leqslant N. \tag{20}$$

Mathematically, the GWS^N is optimal since the approximation error in $q^N(x_j, t)$ is required to be orthogonal to the space of functions supporting q^N for any choice of trial space.

For *any* approximate solution the GWS^N form for (12) is

$$GWS^N = \int_\Omega \Psi_i \left(\frac{\partial q^N}{\partial t} + \frac{\partial}{\partial x_j}(f_j - f_j^{\mathrm{v}})^N \right) \mathrm{d}\tau$$
$$= \int_\Omega \Psi_i \frac{\partial q^N}{\partial t} \, \mathrm{d}\tau - \int_\Omega \frac{\partial \Psi_i}{\partial x_j}(f_j - f_j^{\mathrm{v}})^N \, \mathrm{d}\tau + \int_{\partial\Omega_e \cap \partial\Omega} \Psi_i (f_j - f_j^{\mathrm{v}}) n_j \mathrm{d}\sigma = \{0\}, \tag{21}$$

where the Green–Gauss theorem has been applied to project the divergence operator from the flux vectors f_j and f_j^{v} to the approximation trial space Ψ_i and to produce a surface integral in (21) that is the mathematical placeholder for all *natural* boundary conditions in the GWS^N.

The finite element method uses a spatial semidiscretization (or partitioning) Ω^h of the continuum domain Ω, made up of the union of a set of non-overlapping subdomains Ω_e or finite elements, such that

$$\Omega \approx \Omega^h \equiv \bigcup_e \Omega_e. \tag{22}$$

The approximation q^N is then formed as q^h, the union of finite element approximations q_e on Ω_e, i.e.

$$q(x_j, t) \approx q^N(x_j, t) \equiv q^h(x_j, t) = \bigcup_e q_e(x_j, t). \tag{23}$$

On any finite element domain Ω_e the generic form for q_e is

$$q_e(x_j, t) \equiv \{N_k(\eta_j)\}^{\mathrm{T}} \{Q(t)\}_e, \tag{24}$$

where each element in the row vector $\{N_k\}^{\mathrm{T}}$ (called the finite element *basis* set) is a kth-degree polynomial. There are as many of these polynomials as there are nodal degrees of freedom in Ω_e.

The indicated integrals in (21) are evaluated at the element level and the resulting element-rank expressions are then summed (*assembled*) into a global matrix statement of the form

$$GWS^h = [M]\frac{\mathrm{d}\{Q\}}{\mathrm{d}t} + \{R(Q)\} = \{0\}. \tag{25}$$

In (25), $[M]$ and $\{R\}$ are a global rank square matrix and column vector respectively and $\{Q\} \equiv \{Q(t)\}$ is the array of the state variable approximation coefficients at the geometric nodes of Ω^h. The residual $\{R\}$ is a non-linear function of $\{Q\}$ and contains contributions from all terms in (21) except the time term, i.e. convection, diffusion, source and boundary conditions.

For the present CCM implementation the discretization of the time derivative employs the θ-implicit, one-step (Euler/trapezoidal) algorithm family. The terminal algebraic statement for (25) is of the form

$$\{FQ\} = [M]\{Q_{n+1} - Q_n\} + \Delta t[\theta\{R\}_{n+1} + (1 - \theta)\{R\}_n] = \{0\}, \tag{26}$$

where $t_{n+1} = t_n + \Delta t$ and $0{\cdot}5 \leqslant \theta \leqslant 1{\cdot}0$. A GWS^N is also developed for any Poisson equation in the CCM, directly producing the algebraic system as

$$\{FQ_A\} = [D]\{Q_A\} - \{S_A(Q(t))\}. \tag{27}$$

The GWS^h finite element methodology has therefore produced a coupled, non-linear system of algebraic equations that must be solved iteratively. The classical Newton method constitutes the following iterative cycle:

$$\begin{gathered}\{Q\}_{n+1}^0 = \{Q\}_n, \qquad \{FQ\}_{n+1}^0 = \{FQ\}_n; \quad \text{for } p = 0, 1, 2, \ldots \text{ until convergence,} \\ \left[M + \theta\Delta t \frac{\partial\{R\}}{\partial\{Q\}}\right]_{n+1}^p \{\delta Q\}_{n+1}^{p+1} = -\{FQ\}_{n+1}^p, \qquad \{Q\}_{n+1}^{p+1} = \{Q\}_{n+1}^p + \{\delta Q\}_{n+1}^{p+1}.\end{gathered} \tag{28}$$

Quasi-Newton approximations amount to the use of simplified forms of the Jacobian $[M + \theta\Delta t\partial\{R\}/\partial\{Q\}]$.

The quasi-linear algebraic system (27) has the matrix statement

$$[D]\{Q_A\} = \{S_A(Q(t))\}. \tag{29}$$

REFERENCES

1. B. F. Armaly, F. Durst, J. C. F. Pereira and B. Schönung, 'Experimental and theoretical investigation of backward-facing step flow', *J. Fluid Mech.*, **127**, 473 (1983).
2. D. J. Tritton, *Physical Fluid Dynamics*, 2nd edn, Clarendon, Oxford, 1988.
3. A. J. Baker, 'Finite element solution algorithm for incompressible fluid dynamics', in R. H. Gallagher *et al.* (eds), *Finite Elements in Fluids*, Wiley Interscience, London, 1975, Chap. 4.
4. J. Donea, S. Giuliani and H. Laval, 'Finite element solution of the unsteady Navier–Stokes equations by a fractional step method', *Comput. Methods Appl. Mech. Eng.*, **30**, 53 (1982).
5. O. C. Zienkiewicz, J. Szmelter and J. Peraire, 'Compressible and incompressible flow: an algorithm for all seasons', *Comput. Methods Appl. Mech. Eng.*, **78**, 105 (1990).
6. Z. Fang and I. Paraschivoiu, 'Numerical solutions of the incompressible Navier–Stokes equations with boundary condition switching', *AIAA J.*, **29**, 851 (1991).
7. J. M. Leone Jr and P. M. Gresho, 'Finite element simulations of steady, two-dimensional, viscous incompressible flow over a step', *J. Comput. Phys.*, **41**, 167 (1981).
8. M. G. Carvalho, F. Durst and J. C. F. Pereira, 'Predictions and measurements of laminar flow over two-dimensional obstacles', *Appl. Math. Model.*, **11**, 23 (1987).
9. A. J. Oliver, 'The prediction of turbulent flow and heat transfer over backward facing steps', in K. Morgan *et al.* (eds), *Computer Methods in Fluids*, Pentech, London, pp. 309–337, (1980).
10. J. M. Leone Jr., 'Open boundary condition symposium benchmark solution: stratified flow over a backward facing step', *UCRL-JC-103414 Rev. 1*, Lawrence Livermore National Laboratory, Livermore, CA, 1990.
11. D. K. Gartling, 'A test problem for outflow boundary conditions—flow over a backward-facing step', *Int. j. numer. methods fluids*, **11**, 953 (1990).
12. T. C. Papanastasiou, N. Malamataris and K. Ellwood, 'A new outflow boundary condition', *Int. j. numer. methods fluids*, **14**, 587 (1992).
13. L. K. Kaiktsis, G. E. Karniadakis and S. A. Orszag, 'Onset of three-dimensionality, equilibria, and early transition in flow over a backward-facing step', *J. Fluid Mech.*, **231**, 501 (1991).
14. M. K. Denham and M. A. Patrick, 'Laminar flow over a downstream facing step in a two-dimensional flow channel', *Trans. Inst. Chem. Eng.*, **52**, 361 (1974).
15. L. P. Hackman, G. D. Raithby and A. B. Strong, 'Numerical predictions of flows over backward-facing steps', *Int. j. numer. methods fluids*, **4**, 711 (1984).
16. K. N. Ghia, G. A. Osswald and U. Ghia, 'Analysis of incompressible massively separated viscous flows using unsteady Navier–Stokes equations', *Int. j. numer. methods fluids*, **9**, 1025 (1989).
17. P. T. Williams, 'A three-dimensional, time-accurate, incompressible Navier–Stokes, finite element CFD algorithm', *Ph.D Dissertation*, University of Tennessee, Knoxville, TN, 1993.
18. P. T. Williams and A. J. Baker, 'Incompressible computational fluid dynamics and the continuity constraint method for the three-dimensional Navier–Stokes equations', *Numer. Heat Transfer B*, **29**, 137–273 (1996).
19. P. T. Williams and A. J. Baker, 'A well-posed weak statement algorithm for the pressure Poisson equation for incompressible flows', *AIAA Paper 93-3340-CP*, 1993.
20. W. P. Noronha and A. J. Baker, 'A Taylor weak statement for finite element CFD algorithms for 2D incompressible Navier–Stokes equations', *AIAA Paper 89-0659*, 1989.
21. Y. Saad and M. H. Schultz, 'GMRES: a generalized minimal residual algorithm for solving nonsymmetric linear systems', *SIAM J. Sci. Stat. Comput.*, **7**, 856 (1986).
22. G. H. Golub and C. F. Van Loan, *Matrix Computations*, 2nd edn, Johns Hopkins University Press, Baltimore, MD, 1989.

23. A. J. Baker, P. T. Williams and R. M. Kelso, 'Numerical calculation of room air motion. I. Math. Physics, and CFD modeling', *ASHRAE Trans.*, **100**, 514–530 (1994).
24. P. T. Williams, A. J. Baker and R. M. Kelso, 'Numerical calculation of room air motion. II. The continuity constraint FE method for 3D incompressible thermal flows', *ASHRAE Trans.*, **100**, 531–548(1994).
25. F. M. White, *Viscous Fluid Flow*, McGraw-Hill, New York, 1974.
26. J. Kim and P. Moin, 'Application of a fractional-step method to incompressible Navier–Stokes equations', *J. Comput. Phys.*, **59**, 308 (1985).
27. F. Durst and J. C. F. Pereira, 'Time-dependent laminar backward-facing step flow in a two-dimensional duct', *Trans. ASME J. Fluids Eng.*, **110**, 289 (1988).
28. G. Guj and F. Stella, 'Numerical solutions of high-*Re* recirculating flows in vorticity–velocity form', *Int. j. numer. methods fluids*, **8**, 405 (1988).
29. J. L. Sohn, 'Evaluation of FIDAP on some classical laminar and turbulent benchmarks', *Int. j. numer. methods fluids*, **8**, 1469 (1988).
30. H. C. Ku, R. S. Hirsch, T. D. Taylor and A. P. Rosenberg, 'A pseudospectral matrix element method for solution of three-dimensional incompressible flows and its parallel implementation', *J. Comput. Phys.*, **83**, 260 (1989).
31. S. Thangam and D. D. Knight, 'A computational scheme in generalized coordinates for viscous incompressible flows', *Comput. Fluids*, **18**, 317 (1990).
32. T. Ikohagi and B. R. Shin, 'Finite-difference schemes for steady incompressible Navier–Stokes equations in general curvilinear coordinates', *Comput. Fluids*, **19**, 479 (1991).
33. H. Cabuk, C. H. Sung and V. Modi, 'Explicit Runge–Kutta method for three-dimensional internal incompressible flows', *AIAA J.*, **30**, 2024 (1992).
34. T. Ikohagi, B. R. Shin and H. Daiguji, 'Application of an implicit time-marching scheme to a three-dimensional incompressible flow problem in curvilinear coordinate systems', *Comput. Fluids*, **21**, 163 (1992).
35. E. Steinthorsson, M.-S. Liou, L. A. Povinelli and A. Arnone, 'Numerical simulations of three-dimensional laminar flow over a backward facing step; flow near side walls', *NASA TM 106248*, NASA Lewis Research Center, 1993.
36. B.-N. Jiang, L.-J. Hou and T.-L. Lin, 'Least-sqaures finite element solutions for three-dimensional backward-facing step flow', *NASA TM 106353*, 1993.
37. G. D. Mallinson and G. de Vahl Davis, 'The method of false transient for the solution of coupled elliptic equations', *J. Comput. Phys.*, **12**, 435 (1973).
38. A. A. Amsden and F. H. Harlow, 'The SMAC method: a numerical technique for calculating incompressible fluid flows *LA-4370*, Los Alamos Scientific Laboratory, 1970.
39. G. E. Schneider and G. D. Raithby, 'Finite element analysis of incompressible fluid flow incorporating equal order pressure and velocity interpolation', in K. Morgan *et al.* (eds), *Computer Methods in Fluids*, Pentech, London, pp. 49–83, (1980).
40. P. M. Gresho and R. L. Sani, 'On pressure boundary conditions for the incompressible Navier–Stokes equations', *Int. j. numer. methods eng.*, **7**, 1111 (1987).
41. A. J. Baker and J. W. Kim, 'A Taylor weak-statement algorithm for hyperbolic conservation laws. *Int. j. numer. methods eng.*, **7**, 489 (1987).
42. D. J. Chaffin and A. J. Baker, 'On Taylor weak-statement finite element methods for computational fluid dynamics', *Int. j. numer. methods fluids*, **21**, 273–294 (1995).

